



Liguowuite, WO_3 , a new member of the A-site vacant perovskite type minerals from the Panzhihua–Xichang region, China

Yuan Xue^{1,2}, Ningyue Sun², Hongping He^{3,4}, Aiqing Chen⁵, and Yiping Yang^{3,4}

¹School of Materials Science and Technology,

China University of Geosciences (Beijing), Beijing 100083, PR China

²Crystal Structure Laboratory, Science Research Institute,

China University of Geosciences (Beijing), Beijing 100083, PR China

³CAS Key Laboratory of Mineralogy and Metallogeny,

Guangdong Provincial Key Laboratory of Mineral Physics and Materials,

Guangzhou Institute of Geochemistry, Chinese Academy of Sciences, Guangzhou 510640, PR China

⁴Chinese Academy of Sciences, Beijing 100049, PR China

⁵Analysis and Testing Centre, China Three Gorges University, Yichang 443002, PR China

Correspondence: Yuan Xue (xue.yuea@163.com)

Received: 25 October 2021 – Revised: 20 December 2021 – Accepted: 6 January 2022 – Published: 8 February 2022

Abstract. A new member of the non-stoichiometric perovskite group mineral species, liguowuite, ideally WO_3 , has been found in the Neoproterozoic Sinian biotite-quartz monzonite in the southern part of the Panzhihua–Xichang region (Nanyang village: $26^\circ 46' 8.21''$ N, $101^\circ 27' 13.86''$ E), China. It is associated with hornblende, pargasite, ferro-hornblende, annite, hydrobiotite, phlogopite, orthoclase, microcline, albite, quartz, kaolinite, ilmenite, goethite, hematite, magnetite, pyrite, zircon, zoisite, titanite, epidote, diopside, tourmaline, almandine, fluorapatite, monazite-(Ce), allanite-(Ce), bastnäsite-(Ce), xenotime-(Y), scheelite, moissanite, tellurite, wumuite, and tewite. Liguowuite occurs as greenish yellow prisms, ranging from 0.05 to 0.1 mm in diameter, and it is transparent with a greasy luster and a white streak. Liguowuite exhibits a triclinic pseudomorphism composed of nanoparticles with many cracks and nanovoids. This mineral is brittle and has a Mohs hardness value of approximately 3–4. The calculated density is 7.22 g cm^{-3} . Electron microprobe analyses gave (average weight percent, wt %, of 15 spot analyses of 4 samples) $\text{K}_2\text{O} = 0.01$, $\text{WO}_3 = 99.23$, $\text{TeO}_2 = 0.03$, $\text{CaO} = 0.06$, $\text{Na}_2\text{O} = 0.04$, and total 99.37, yielding the empirical formula $\text{W}_{1.00}\text{O}_3$, based on $\text{O}_{\text{apfu}} = 3$ and ideally WO_3 . The strongest five diffraction lines (d Å (I)(hkl)) are 3.8552 (88)(002), 3.7685 (88)(020), 3.6590 (100)(–200), 2.6928 (43)(022), and 2.6258 (60)(202). Liguowuite is monoclinic and is in space group $P2_1/n$, with $a = 7.32582(18)$ Å, $b = 7.54767(18)$ Å, $c = 7.71128(18)$ Å, $\beta = 90.678(3)^\circ$, $V = 426.348(19)$ Å³, and $Z = 8$. The crystal structure data were refined using the Rietveld refinement method and X-ray powder diffraction data. The reliability factors (R factors) were $R_{\text{wp}} = 0.0604$ and $R_{\text{p}} = 0.0454$, with $\chi^2 = 1.707$. Liguowuite consists of corner-sharing distorted and tilted $[\text{WO}_6]$ octahedra, in which the W atoms are off-center and form six W–O bonds ranging from 1.7 to 2.2 Å with the surrounding oxygen atoms. According to the hierarchical scheme for perovskite supergroup minerals, liguowuite is the first reported example of A-site vacant single oxide, i.e., a new perovskite subgroup.

1 Introduction

A new mineral species of perovskite supergroup, liguowuite, ideally WO_3 , was discovered in a sample of new minerals (tewite and wumuite) from the Pan–Xi (Panzhuhua–Xichang) region, Southwest China. The suggested Strunz classification is 04.EA.10, 04-OXIDES (hydroxides, vanadates, arsenites, antimonites, bismuthites, sulfites, selenites, tellurites, and iodates). The Dana classification is 04.05.01.02, 04 oxide minerals.

The perovskite supergroup minerals defined by Mitchell et al. (2017) refer to minerals of ABX_3 compounds with $A = A$ site; $B = B$ site; and $X = \text{O}, \text{F},$ and Cl but also OH and As . Their structures are composed of three-dimensional networks of tilted and/or distorted corner-sharing octahedra, and they have an aristotypic ABX_3 perovskite structure or its derivatives. The B -site cations can be randomly distributed and defined as single perovskite (ABX_3) or ordered and defined as double perovskite ($\text{A}_2\text{BB}'\text{X}_6$). The A and B sites can be partially or entirely vacant. The perovskite supergroup is divided into stoichiometric and non-stoichiometric perovskite groups, which can both be further classified into single or double perovskite. Subgroups and potential subgroups of non-stoichiometric perovskites involve (1) A -site vacant hydroxide or double hydroxide perovskites, (2) A -site vacant quadruple perovskites, (3) B -site vacant single perovskites, (4) B -site vacant inverse single perovskites, (5) B -site vacant double perovskites, (6) anion-deficient partly inverse B -site quadruple perovskites, and (7) anion-deficient perovskites.

The application of the hierarchical scheme for perovskite supergroup minerals proposed by Mitchell et al. (2017) results in the identification of a perovskite supergroup including about 17 subgroups and 47 mineral species. According to this hierarchical scheme, liguowuite belongs to the non-stoichiometric perovskite group and is the first reported example of A -site vacant single perovskite as an oxide mineral for this group, i.e., a new subgroup.

Chesnokov et al. (1998) used to report “krasnogorite” (formula: WO_3 ; space group: $Pmnb$) occurring as pseudomorphs after hard alloy VK8 (a type of artificial alloy) on the plates of the cutting element of a drilling machine found in burned rocks. But it is invalid because current International Mineralogical Association (IMA) regulations do not allow such substances associated with human factors to be approved as valid mineral species. The liguowuite found in this study is naturally formed nano-monoclinic WO_3 .

The mineral was named liguowuite after Li Guowu (1964–) in recognition of his great contributions to new mineral research, including tewite and wumuite in this area. The new mineral and the mineral name have been approved by the International Mineralogical Association Commission on New Minerals, Nomenclature, and Classification (IMA-CNMNC) (IMA2020-097). Type material has been deposited at the China University of Geosciences (Beijing) Museum, Beijing, PR China, under registration number 21K005, and at the Ge-

ological Museum of China (15 Xisi Mutton Alley, Beijing, PR China) under registration number M16121.

2 Sample description

2.1 Geological background

Liguowuite was discovered in the vicinity of the village of Nanyang, Huaping County, Yunnan Province ($26^\circ 46' 18.21'' \text{N}$, $101^\circ 27' 13.86'' \text{E}$), southern Panzhuhua–Xichang region, Southwest China (Fig. 1). The mineral occurs in Neoproterozoic Sinian semi-weathered biotite adamellite, and the rock mass's edge is near the contact zone with Permian basites. An independent sulfide-type tellurium deposit related to hydrothermal activity has been discovered in the Dashuigou sulfide ore in Shimian County, northern Pan–Xi region (Chen et al., 1994; Li et al., 2019). A quartz vein gold deposit 300 m south of the location for the liguowuite was found within a fault zone in Permian mafic rocks (gabbro). Although the liguowuite was found in the Proterozoic monzonitic rocks, the mineral formation process may be related to this nearby pyrite quartz vein-type gold mineralization in the younger basic rocks. The high-temperature fluids of the gold mineralization are rich in W , Te , and Au . The minerals crystallized and filled the fissures in the monzonitic rocks.

Liguowuite was found as extremely rare grains in heavy mineral concentrates. It was associated with hornblende, pargasite, ferro-hornblende, annite, hydrobiotite, phlogopite, orthoclase, microcline, albite, quartz, kaolinite, ilmenite, goethite, hematite, magnetite, pyrite, zircon, zoisite, titanite, epidote, diopside, tourmaline, almandine, fluorapatite, monazite-(Ce), allanite-(Ce), bastnäsite-(Ce), xenotime-(Y), scheelite, moissanite, tellurite, tewite (IMA2014-053), and wumuite (IMA2017-067a).

2.2 Occurrence and physical and optical properties

Liguowuite occurs as greenish yellow prismatic grains, and it is translucent with a greasy luster and a white streak (Fig. 2). As is shown in back-scattered electron (BSE) images (Fig. 2), liguowuite exhibits a triclinic appearance and pseudomorphism (0.05 to 0.1 mm in diameter). It is composed of nanoparticles with many cracks and nanovoids. The nanoparticle size varies from 100 to 200 nm. It is brittle with uneven fractures. No cleavage or parting was observed. This mineral has a Mohs hardness of about 3–4 and a calculated density of 7.22 g cm^{-3} based on the empirical formula and unit cell volume refined from the X-ray powder diffraction data. An average refraction index of 2.24 was calculated based on the Gladstone–Dale relationship and its composition (Mandarino, 1981). The sample is non-fluorescent.

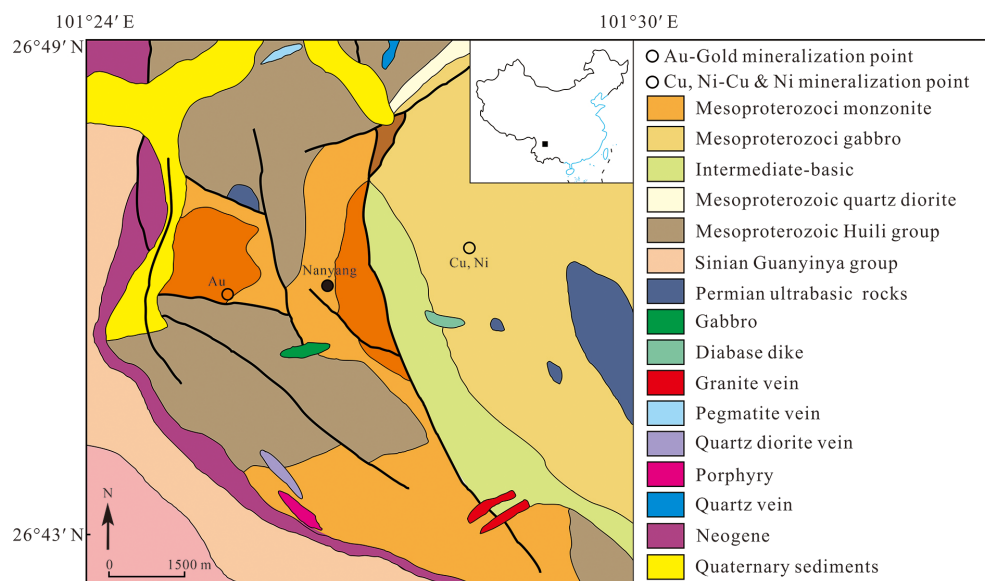


Figure 1. Geologic map of the locality. Modified from Li et al. (2019).

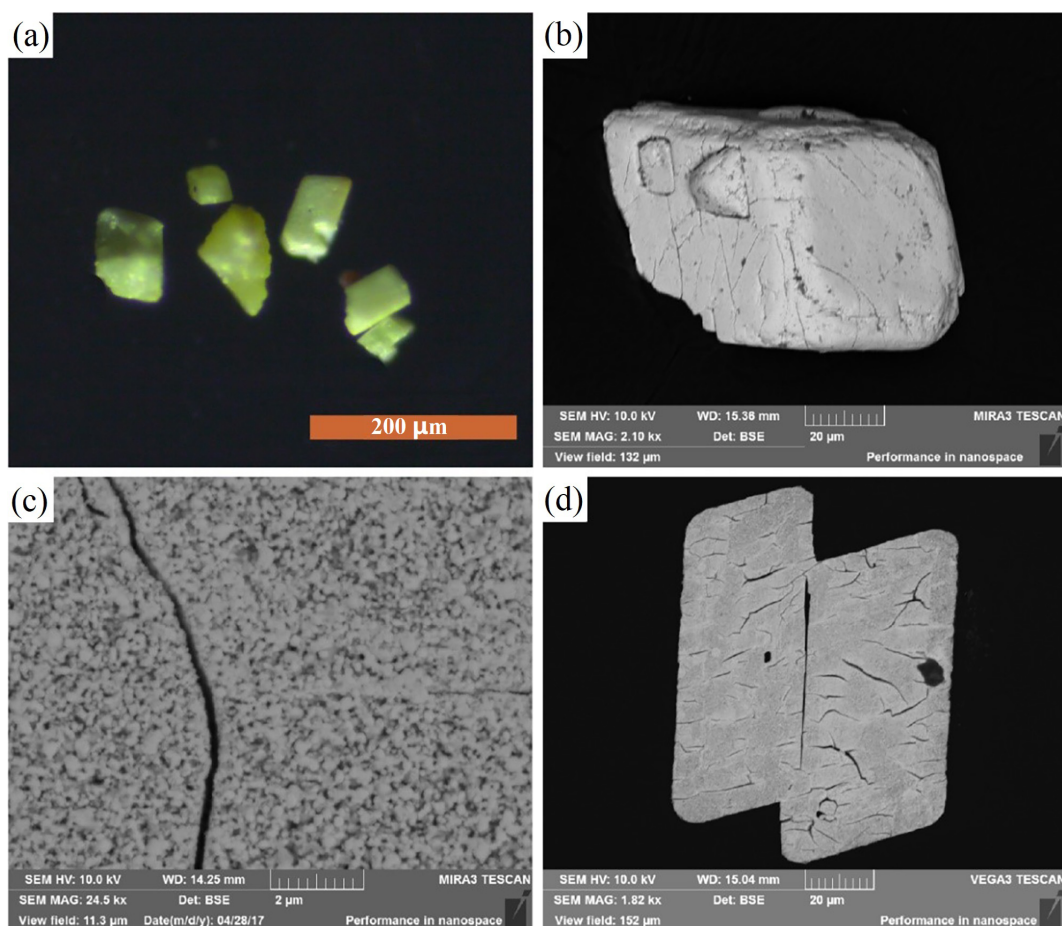


Figure 2. Photos and back-scattered electron (BSE) images of the liguowuite. (a) Yellow grains of liguowuite, (b) BSE images of a liguowuite aggregate grain, (c, d) BSE images of a polished face. The liguowuite grain is composed of nanoparticles with many cracks and nanovoids.

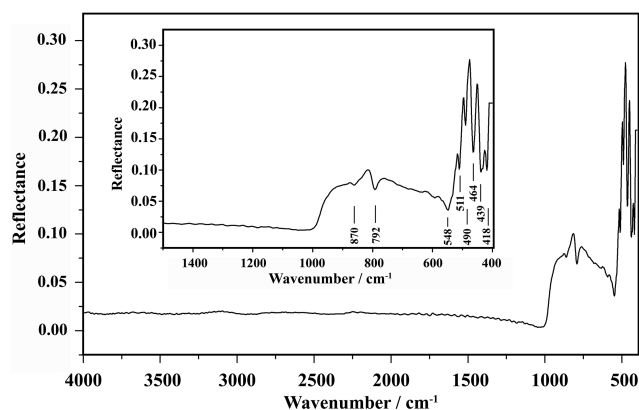


Figure 3. The IR spectrum of liguowuite.

3 Methods

3.1 Electron microprobe analysis (EMPA)

The composition of the liguowuite was determined via wavelength-dispersive spectroscopy at the Beijing Research Institute of Uranium Geology (BRIUG) using a JEOL JXA-8100 electron microprobe, with an accelerating voltage of 20 kV, a beam current of 10 nA, and a 2 μm beam diameter. The standards analyzed included albite for Na, Ca, and Al; scheelite for W; microcline for K; and Sb_2Te_3 for Te.

3.2 Infrared spectra

The infrared (IR) spectrum of liguowuite (Fig. 3) was acquired with the polished face of an aggregate grain using a Bruker HYPERION 1000 FTIR microscope operated in reflection mode. The spectrum data were processed using the OPUS software (Bruker Optics, 2019) during a 32-cycle scan at a resolution of 4 cm^{-1} . The samples were kept at 110 $^\circ\text{C}$ for 2 h in a drying oven before the test to avoid the effect of adsorbed water on the test results.

3.3 Raman spectra

The Raman spectrum (Fig. 4) of the liguowuite was obtained using a RENISHAW in a Via-Reflex spectrometer, with a laser excitation wavelength of 532 nm. The spectrum in the 100–3200 cm^{-1} region was obtained using a collection time of 10.00 s with the polished grain described above.

3.4 Powder X-ray diffraction

As is shown in Fig. 2c, the liguowuite crystal is composed of nanoparticles less than 200 nm in diameter, so it is difficult to obtain single-crystal X-ray diffraction data (Fig. 5). The crystal structure was refined using the Rietveld refinement method and X-ray powder diffraction data.

Owing to the lack of samples, the X-ray powder diffraction data were collected twice using single-crystal diffrac-

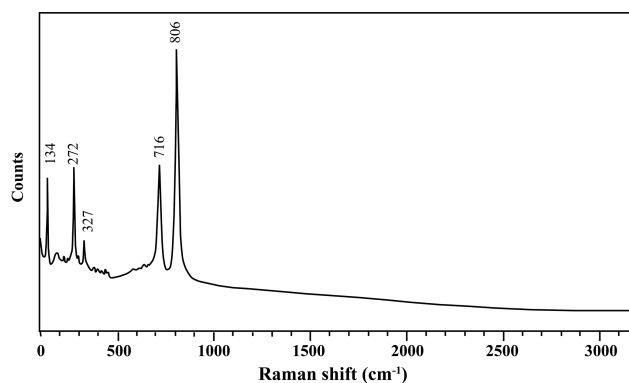


Figure 4. The Raman spectrum of liguowuite.

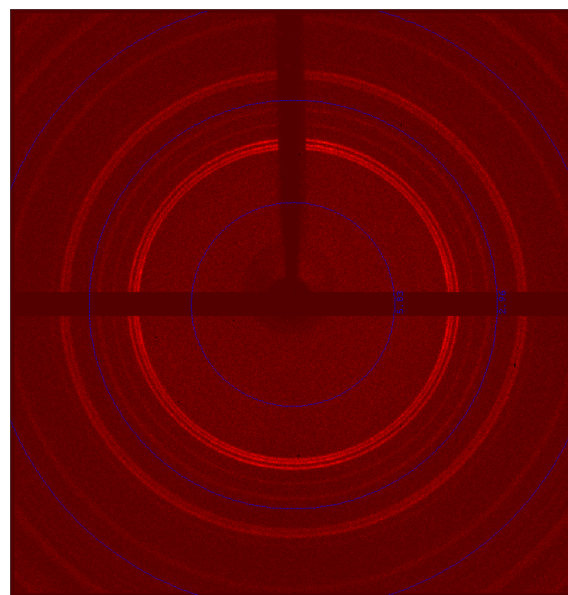


Figure 5. X-ray diffraction image of a triclinic grain of liguowuite ($\text{Mo K}\alpha$).

tometers. The first study involved the use of a Rigaku Oxford diffraction XtaLAB PRO-007HF rotating anode microfocus X-ray source (50 kV, 24 mA, 1.2 kW, $\text{Mo K}\alpha$, and exposure time of 500 s) with a hybrid pixel array detector and a single-crystal diffractometer. The second study adopted a single-crystal diffractometer with a 2D detector system (PHOTON III CPAD detector, Bruker D8 VENTURE) equipped with a kappa geometry-based goniometer 2D detector and the XRD 2D scan software APEX3 (Francart et al., 2008), with a 0.1 \times 0.1 \times 0.1 mm grain. A Cu Incoatec Microfocus Source I μs generated the X-ray beam ($\text{Cu K}\alpha$, $\lambda = 1.5418 \text{ \AA}$). Two 2D diffraction patterns were collected using the detector at positions $2\theta = -15$ and -30° , with an exposure time of 120 s ($\Phi 360^\circ$).

Table 1. Chemical data (wt %) for liguowuite.

Constituent	Average	Range	SD	Reference material
Al ₂ O ₃	n.d.	n.d.–0.01	n.d.	Albite
WO ₃	99.23	98.19–99.93	0.53	Scheelite
K ₂ O	0.01	n.d.–0.05	0.02	Microcline
TeO ₂	0.03	n.d.–0.14	0.04	Sb ₂ Te ₃
CaO	0.06	n.d.–0.11	0.03	Albite
Na ₂ O	0.04	n.d.–0.10	0.03	Albite
Total	99.37	98.35–100.13	0.52	

SD: standard deviation; n.d.: not detected.

3.5 Transmission electron microscope (TEM)

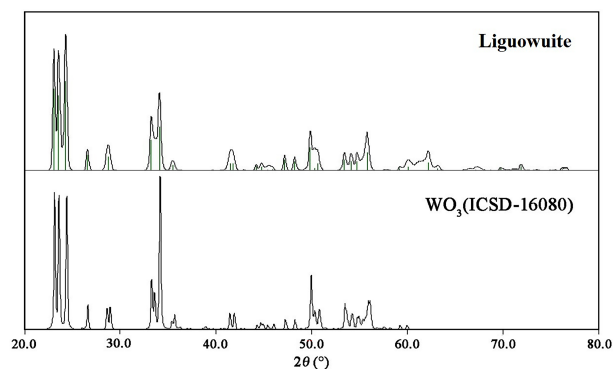
The transmission electron microscopy (TEM) observations were performed using an FEI Talos F200S scanning and transmission electron microscope at a 200 kV accelerating voltage, equipped with an X-ray energy-dispersive detector at the Guangzhou Institute of Geochemistry, Chinese Academy of Sciences, China. The specimen was prepared by adding crushed powder to ethanol and ultrasonically dispersing the powder for 10 min. A droplet of the resultant dispersion was deposited on a carbon-coated copper microgrid and was naturally dried at room temperature. High-resolution transmission electron microscope (HRTEM) images and selected area electron diffraction (SAED) patterns were obtained via TEM. Compositional mapping scanning of nanocrystallites of liguowuite was conducted using energy-dispersive spectroscopy (EDS) under the following conditions: a 200 kV accelerating voltage, a 1 nA beam current, and a beam size of ~ 5 nm in STEM mode.

4 Results

4.1 Chemical composition

The results of electron microprobe analyses of 15 spots on 4 grains are summarized in Table 1. The total amount of the electron microprobe analysis varies within a certain range (Table 1), but the IR and Raman spectra reveal that H₂O or OH⁻ does not exist in liguowuite. In addition, compared with synthetic materials and natural tungsten oxide hydrate minerals, the powder diffraction pattern of liguowuite is much closer to that of synthetic WO₃. The compositional analyses show that liguowuite contains 99.23 (98.19–99.93) wt % WO₃, 0.06 (0–0.11) wt % CaO, 0.04 (0–0.10) wt % Na₂O, 0.03 (0–0.14) wt % TeO₂, and 0.01 (0–0.05) wt % K₂O.

The empirical formula calculated on the basis of O_{apfu} = 3 is W_{1.00}O₃. The simplified end-member formula is WO₃.

**Figure 6.** X-ray powder diffraction pattern of liguowuite (Cu K α).

4.2 Spectroscopic characteristics

4.2.1 Infrared spectra

The IR spectrum for liguowuite is shown in Fig. 3. The bands at 870 and 792 cm⁻¹ represent stretching modes of the [WO₆] octahedron, and the bands at 548, 511, 490, 464, 439, and 418 cm⁻¹ correspond to W–O bending vibrations (Gadsden, 1975; Farmer, 1982; Xue et al., 2020).

4.2.2 Raman spectra

The Raman spectrum of liguowuite is shown in Fig. 4, and it is quite consistent with the spectrum of synthetic WO₃ in the KnowItAll database. The band at 134 cm⁻¹ represents the lattice mode. The 272 and 327 cm⁻¹ bands could be assigned to δ (O–W–O). The bands at 716 and 806 cm⁻¹ could be assigned to ν (O–W–O) (Daniel et al., 1987).

4.3 Crystal structure

4.3.1 Powder X-ray diffraction

X-ray powder diffraction data and the pattern of liguowuite (Cu K α) are presented in Table 2 and Fig. 6. The five strongest diffraction lines (d Å (I)(hkl)) include 3.8552 (88)(002), 3.7685 (88)(020), 3.6590 (100)(-200), 2.6928 (43)(022), and 2.6258 (60)(202).

The phase identification was performed using the Search-match software (Oxford Cryosystems Ltd., 1999), and the X-ray diffraction pattern of liguowuite corresponds to that of synthetic monoclinic WO₃ (ICSD 16080, $P2_1/n$ (no. 14)) (Fig. 6). Based on the XRD pattern, 44 diffraction peaks were assigned to liguowuite. The index process was conducted using the CheckCell software (Laugier and Bochu, 2000), and all 44 of the diffraction peaks matched were successfully indexed. The unit cell parameters refined using the powder data are as follows: $a = 7.32582(18)$ Å, $b = 7.54767(18)$ Å, $c = 7.71128(18)$ Å, $\beta = 90.678(3)^\circ$, $V = 426.348(19)$ Å³, and $Z = 8$.

Table 2. X-ray powder diffraction data (d in Å) for liguowuite.

I_{meas}	d_{meas}	d_{calc}	h	k	l	I_{meas}	d_{meas}	d_{calc}	h	k	l
<1	4.3363	4.3553	-1	1	1	16	1.7133	1.7126	0	2	4
88	3.8552	3.8455	0	0	2	14	1.6925	1.6917	0	4	2
88	3.7685	3.7675	0	2	0	13	1.6749	1.6743	2	4	0
100	3.6590	3.654	-2	0	0	27	1.6455	1.6457	1	4	2
<1	3.4368	3.4252	0	1	2	1	1.5956	1.5982	-3	3	2
18	3.3515	3.3487	-1	2	0	3	1.5589	1.5586	-2	2	4
20	3.1040	3.1172	-1	1	2	6	1.5386	1.5389	-2	4	2
43	2.6928	2.6912	0	2	2	12	1.4908	1.4902	-3	4	0
60	2.6258	2.6296	2	0	2	3	1.4694	1.4698	3	1	4
8	2.5273	2.5339	-1	2	2	1	1.4153	1.4146	-2	3	4
<1	2.4681	2.4746	2	2	1	1	1.4042	1.4031	0	5	2
<1	2.4118	2.4081	1	0	3	2	1.3909	1.3924	3	2	4
1	2.2682	2.2664	1	3	1	<1	1.3632	1.3626	-5	2	0
2	2.1047	2.1029	0	3	2	3	1.3459	1.3456	0	4	4
6	2.0477	2.0456	-3	2	0	<1	1.3345	1.3343	-4	0	4
6	2.0225	2.0252	-1	3	2	<1	1.3245	1.3258	-1	4	4
1	1.9923	1.9945	2	3	1	5	1.3118	1.3115	-4	4	0
2	1.9774	1.9729	3	1	2	1	1.2994	1.2992	0	5	3
14	1.9242	1.9228	0	0	4	1	1.2860	1.2869	3	3	4
13	1.8849	1.8837	0	4	0	1	1.2656	1.2657	-3	5	1
32	1.8273	1.8270	-4	0	0	1	1.2581	1.2578	-4	2	4
12	1.8007	1.7992	1	1	4	2	1.2482	1.2483	-1	1	6

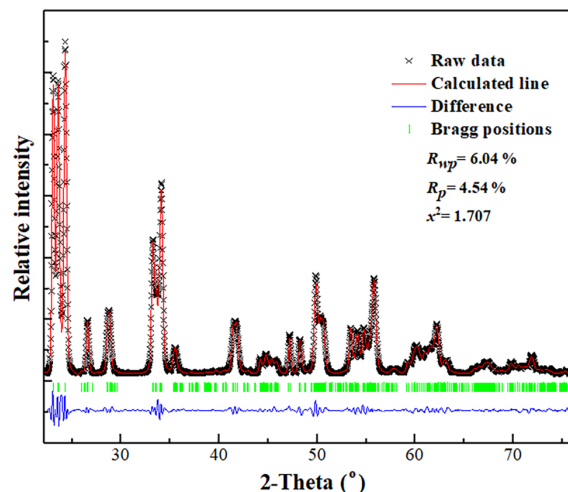
Note: the five strongest lines are in bold.

Table 3. The atom coordinates of liguowuite. “Wyck” signifies Wyckoff, and “Occ” signifies occupancy.

Atom	Wyck.	Occ.	x/a	y/b	z/c
W1	4e	1	0.2467(3)	0.0281(2)	0.2866(2)
W2	4e	1	0.2548(3)	0.0345(2)	0.7813(2)
O1	4e	1	0.0025	0.0350	0.2106
O2	4e	1	0.9974	0.4636	0.2161
O3	4e	1	0.2840	0.2605	0.2848
O4	4e	1	0.2099	0.2568	0.7318
O5	4e	1	0.2827	0.0383	0.0046
O6	4e	1	0.2856	0.4840	0.9944

Rietveld powder structure refinement was conducted using the GSAS (General Structure Analysis System) software (Larson and Von Dreele, 1994) and crystal structure model data from ICSD 16080. The reliability factors (R factors) were $R_{\text{wp}} = 0.0604$ and $R_p = 0.0454$, with $\chi^2 = 1.707$. The fitting results of the Rietveld refinement in space group $P2_1/n$ are shown in Fig. 7. The atom coordinates and selected geometric parameters are listed in Tables 3 and 4.

The bond-valence sums (BVSs) were calculated using the interatomic distances following the procedure of Brown (1977) and using the parameters of Hong et al. (2004). The BVSs for the W1 and W2 positions are 6.033 and 6.195 valence units (v.u.), and those for the O1, O2, O3, O4, O5,

**Figure 7.** Fitting results of the Rietveld analysis in space group $P2_1/n$.

and O6 positions are 1.951, 2.074, 2.009, 2.090, 2.058, and 2.046 v.u., respectively, which are comparable to the expected values. Furthermore, all of the resulting BVS values are in agreement with the ideal values (Table 5), and the results meet the charge balance requirement.

Table 4. Selected geometric parameters (Å, °) for liguowuite.

W1–O1	1.8765(24)	W2–O1	1.9585(22)
W1–O2	1.9374(24)	W2–O2	1.8525(23)
W1–O3(1)	1.7750(18)	W2–O4(1)	1.7508(17)
W1–O3(2)	2.1050(18)	W2–O4(2)	2.1146(16)
W1–O5	2.1948(16)	W2–O5	1.7322(17)
W1–O6	1.7404(16)	W2–O6	2.1763(16)
< W1–O >	1.938	< W2–O >	1.931
O1–W1–O2	157.32(10)	O1–W2–O2	159.64(10)
O1–W1–O3	96.70(10)	O1–W2–O4	94.89(10)
O1–W1–O3(2)	81.16(8)	O1–W2–O4(2)	81.61(7)
O1–W1–O5	79.34(6)	O1–W2–O5	94.28(9)
O1–W1–O6	99.69(11)	O1–W2–O6	82.21(7)
O2–W1–O3	95.70(10)	O2–W2–O4	96.43(9)
O2–W1–O3(2)	81.74(7)	O2–W2–O4(2)	82.91(8)
O2–W1–O5	82.56(7)	O2–W2–O5	99.63(10)
O2–W1–O6	96.02(9)	O2–W2–O6	81.74(7)
O3–W1–O3	164.17(9)	O4–W2–O4	164.21(10)
O3–W1–O5	86.42(7)	O4–W2–O5	102.74(8)
O3–W1–O5(2)	77.77(5)	O4–W2–O5(2)	92.90(7)
O3–W1–O6	102.67(8)	O4–W2–O6	86.11(7)
O3–W1–O6(2)	93.14(8)	O4–W2–O6(2)	78.18(5)
O5–W1–O6	170.90(11)	O5–W2–O6	170.78(10)
< O–W–O >			
W1–O1–W2	153.76(8)	W2–O4–W2	159.63(1)
W1–O2–W2	158.83(8)	W1–O5–W2	166.01(10)
W1–O3–W1	159.09(1)	W1–O6–O2	153.61(8)
< W–O–W >			

Table 5. Bond-valence sum for liguowuite.

	W1	W2	O sum
O1	1.083 × 1 ↓→	0.868 × 1 ↓→	1.951
O2	0.919 × 1 ↓→	1.156 × 1 ↓→	2.074
O3(1)	1.425 × 1 ↓→		2.009
O3(2)	0.584 × 1 ↓→		
O4(1)		1.521 × 1 ↓→	2.090
O4(2)		0.569 × 1 ↓→	
O5	0.458 × 1 ↓→	1.600 × 1 ↓→	2.058
O6	1.565 × 1 ↓→	0.482 × 1 ↓→	2.046
Sum	6.033	6.195	

Note: the bond-valence sums were calculated using the equation and constants of Brown (1977) ($S = \exp(R_0 - d_0)/b$) and bond parameters for W⁶⁺–O from Hong et al. (2004). The symbols → and ↓ mean that the value should be summed horizontally and vertically, respectively.

4.3.2 Transmission electron microscope (TEM)

The nanocrystallites of the liguowuite were analyzed using transmission electron microscopy combined with energy-dispersive spectroscopy (EDS) to confirm their compositions (Fig. 8). The EDS element maps reveal that the W, O, Te, Na, and Ca are evenly distributed throughout the particle (Fig. 8).

These nanocrystallites were further characterized using TEM and selected area electron diffraction (SAED) (Fig. 9).

Figure 10 shows electron diffraction patterns of the [010] and [10–1] zone axes of liguowuite. Using space group $P2_1/n$ (no. 14) and the monoclinic cell parameters, all of the intense reflections in the directions of the [010] and [10–1] zone axes were successfully indexed and are consistent with the electron diffraction simulation. Most of the reflections accord with the systematic absence condition of glide plane n ($h + l \neq 2n$ ($k = 0$)). The presence of several weak reflections with $h + l \neq 2n$ in the SAED pattern and the absence of these types of reflections in the PXRD pattern (Fig. 6) indicate short-range ordering in the liguowuite structure, but generally the structure is in agreement with the $P2_1/n$ model. Based on the indexed data, $d(200) = 0.37126$ nm, $d(020) = 0.37586$ nm, and $d(002) = 0.38682$ nm were obtained, so the calculated axis lengths based on the electron diffraction data are $a = 0.74252$ nm, $b = 0.75174$ nm, and $c = 0.77365$ nm, which are close to those obtained from the powder crystal refinement. The lattice fringes of the liguowuite with spacings of 0.3773 and 0.4375 nm, which correspond to the {020} and {111} planes, respectively, were observed using high-resolution TEM (Fig. 9b).

4.3.3 Crystal structure characteristics

A schematic projection view of the liguowuite crystal structure is shown in Fig. 11. The structure is composed of corner-sharing distorted and tilted [WO₆] octahedra to form a three-dimensional network containing large 12-fold coordinated cavities. The W atoms in [WO₆] octahedra are off-center and form six W–O bonds ranging from 1.7 to 2.2 Å with the surrounding oxygen atoms. The structure is derived from the perovskite- or ReO₃-type structures (Hyde and Andersson, 1989).

Based on the model reported in the ICSD 16080, our study confirmed that liguowuite is characterized by (1) tilting and distortion of the corner-sharing BX_6 octahedra, (2) disordering of the B-site cations, and (3) the formation of A-site vacancies. According to the hierarchical scheme, liguowuite is a member of the perovskite supergroup minerals, in the form of the first example of an A-cation-free single perovskite as an oxide mineral, i.e., a new subgroup of the non-stoichiometric perovskite group. A revised version of the hierarchical categories of the non-stoichiometric perovskite subgroup minerals is provided in Fig. 12 based on the original version of Mitchell et al. (2017).

5 Discussion

5.1 [WO₆] octahedra framework of WO₃

Although liguowuite was discovered as a rare new mineral, artificial WO₃ is a common material with a variety of structural symmetries. For comparison, comparable synthetic phases are listed in Table 6. WO₃ can be regarded as a [WO₆] octahedra framework joined by corners and the ba-

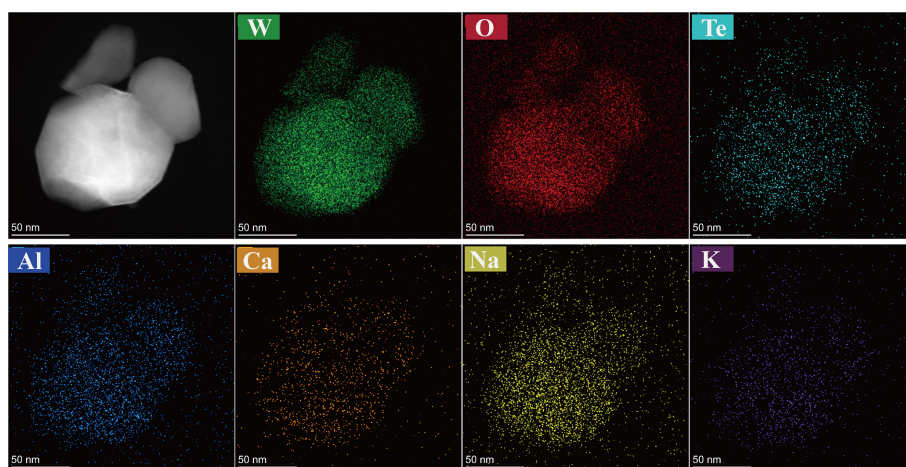


Figure 8. Energy-dispersive spectroscopy (EDS) element maps of the major elements, including W and O, as well as the minor elements Te, Na, K, Ca, and Al.

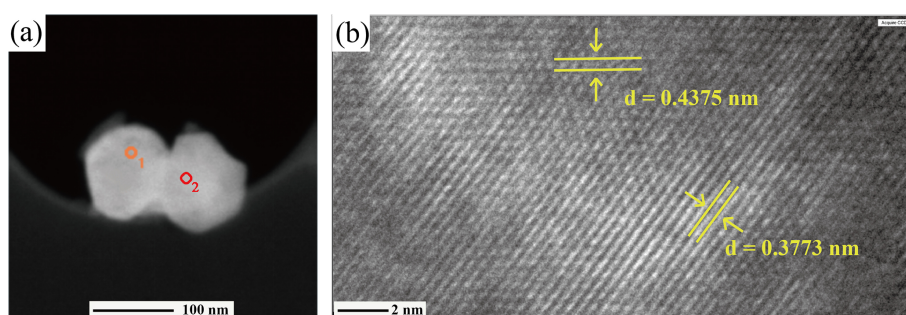


Figure 9. TEM images of liguowuite. (a) High-angle annular dark field (HAADF) image of the analyzed nanocrystals. The selected electron diffraction results for the circle 1 and circle 2 regions are shown in Fig. 10a and b, respectively. (b) The HRTEM image of the right particle in Fig. 9a, with lattice fringe spacings of 0.3773 and 0.4375 nm corresponding to the $\{020\}$ and $\{111\}$ planes, respectively.

sic structure of tungsten bronze compounds. By comparing the crystal structure characteristics of synthetic WO_3 materials, the $[\text{WO}_6]$ framework commonly forms trigonal, square, rhombic, irregular pentagon, or hexagonal tunnels. The structures are mainly pyrochlore-type, perovskite-type, and typical tungsten-bronze-type, and all can be viewed as being made up of a slab structure.

From the projection onto (001) of the hexagonal tungsten bronze (HTB) (Fig. 13a), tetragonal tungsten bronze (TTB) (Fig. 13b), and orthorhombic tungsten bronze (OTB) (Fig. 13c), 1D tunnels including trigonal + hexagonal tunnels, trigonal + square + irregular pentagon tunnels, and trigonal + hexagonal tunnels can be observed running along the c axis, respectively. The tungsten bronze slab structure consists of $[\text{WO}_6]$ octahedra layers with a hexagonal, tetragonal, or orthorhombic tungsten bronze topology and a thickness of 3.7–3.9 Å. These structural slabs connect to each other directly as they do in the perovskite structure, whereas only square or rhombic tunnels can be observed on (100), (010), and (001) in the perovskite structure (Fig. 13d).

The cubic WO_3 phase has a pyrochlore-type structure with empty 3D tunnels. The structure can be described as distorted (001) layers of hexagonal WO_3 linked along the [111] direction, and 3D interconnected tunnels are formed (Fig. 13e). The pyrochlore slab is composed of two types of trigonal layers, with a thickness of about 6 Å.

If the 6 Å wide pyrochlore slabs are indicated by Py and the 3.7–3.9 Å wide tungsten bronze/perovskite slabs by TB/Per, then the translational repeat of the pyrochlore structure is $\langle \text{Py} \rangle$, tungsten bronze is $\langle \text{TB} \rangle$, and perovskite is $\langle \text{Per} \rangle$. In these three cases, the slab framework is composed of corner-sharing $[\text{WO}_6]$ octahedra, so the WO_3 stoichiometry of the framework is consistent.

Tungsten bronze specifically refers to a non-stoichiometric compound with a general formula of $A_x\text{WO}_3$ ($0 < x < 1$). However, as more and more minerals with such a chemical formula are found, the tungsten bronze structure is not an accurate concept from a mineralogical point of view. Minerals with a $[\text{WO}_6]$ octahedra corner-sharing framework should be divided into perovskite-type structure, such as liguowuite;

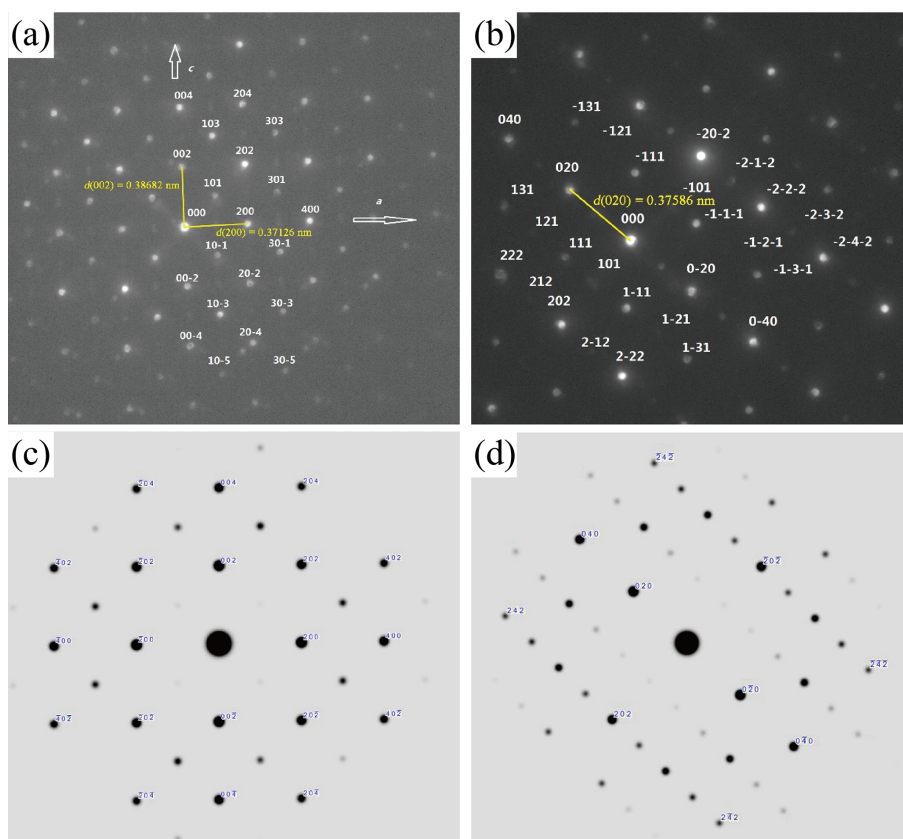


Figure 10. Selected area electron diffraction (SAED) patterns and calculated patterns for liguowuite; (a) [010] zone axis electron diffraction pattern and indexation of the liguowuite structure (the reflection condition of glide plane n is $h + l = 2n$ ($k = 0$); weak extra $h + l \neq 2n$ reflections are marked in light blue.); (b) [10–1] zone axis electron diffraction pattern and indexation of the liguowuite structure; (c) [010] zone axis electron diffraction simulation calculated using the $P2_1/n$ model; (d) [10–1] zone axis electron diffraction simulation calculated using the $P2_1/n$ model.

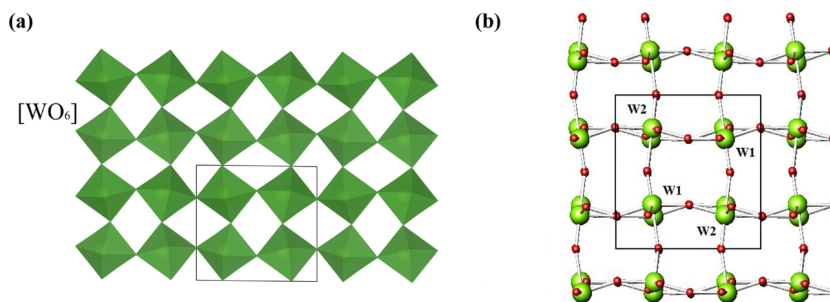


Figure 11. The crystal structure of liguowuite. $[\text{WO}_6]$ octahedra are shown in green. Green and red balls correspond to W and O atoms, respectively.

pyrochlore-type structure, such as hydrokenoelsmoreite; or tungsten bronze structure, such as wumuite.

5.2 Genesis of liguowuite

Research on monoclinic nano- WO_3 films and powders has generated interest because of their photocatalytic applications (Guo et al., 2007; Martínez et al., 2007; Shang et al.,

2020; Sirotkin et al., 2020), photochromic behavior (Poirier et al., 2007; Miyazaki et al., 2015; Evdokimova et al., 2019), and use in semiconducting metal oxide (SMO)-based sensors for detecting gaseous adsorbates (Li et al., 2004; Reyes et al., 2006; Khadayate et al., 2007; Akamatsu et al., 2013; Tian et al., 2014; Yang et al., 2014; Gui et al., 2016).

Various synthetic methods of fabricating nano-sized monoclinic WO_3 ($m\text{-WO}_3$) particles have recently been reported

Table 6. Data for comparison of liguowuite with related synthetic materials.

No.	Name	Formula	Z	Space group	<i>a</i> (Å)	<i>b</i> (Å)	<i>c</i> (Å)	α	β	γ
This work	Liguowuite	WO ₃	8	<i>P2₁/n</i>	7.3258(1)	7.5476(1)	7.7112(1)	90	90.678(3)	90
7081	Tungsten oxide	WO ₃	8	<i>P2₁/n</i>	7.306(1)	7.540(1)	7.692(1)	90	90.881(5)	90
42778	Tungsten oxide	WO ₃	4	<i>P2₁/c</i>	5.261(2)	5.128(1)	7.650(4)	90	92.05(3)	90
15102	Tungsten oxide	WO ₃	4	<i>P2₁/a</i>	7.274(2)	7.501(1)	3.824(3)	90	89.93	90
42085	Tungsten oxide	WO ₃	4	<i>Pc</i>	5.27710(1)	5.15541(1)	7.66297(1)	90	91.7590(2)	90
6218	Tungsten oxide	WO ₃	8	<i>Pmnb</i>	7.341(4)	7.570(4)	7.754(4)	90	90	90
53573	Tungsten oxide	WO ₃	8	<i>Pcnb</i>	7.3331(2)	7.5733(2)	7.7401(3)	90	90	90
38828	Tungsten oxide	WO ₃	8	<i>P$\bar{1}$</i>	7.31261(6)	7.52521(7)	7.68937(7)	88.847	90.912	90.94
39331	Tungsten oxide	WO ₃	6	<i>P6₃/mcm</i>	7.3244(6)	7.3244(6)	7.6628(5)	90	90	120
15220	Tungsten oxide	WO ₃	3	<i>P6/mmm</i>	7.298(2)	7.298(2)	3.899(2)	90	90	120
44841	Tungsten oxide	WO ₃	4	<i>P4$\bar{2}$₁m</i>	7.39(2)	7.39(2)	3.88(1)	90	90	90
58807	Tungsten oxide	WO ₃	2	<i>P4/nmm</i>	7.86(1)	7.86(1)	7.49(1)	90	90	90
11365	Tungsten oxide	WO ₃	2	<i>P4/nmm</i>	5.272(2)	5.272(2)	3.920(2)	90	90	90
57893	Tungsten oxide	WO ₃	4	<i>P4/ncc</i>	5.2885(5)	5.2885(5)	7.8626(8)	90	90	90
*	Tungsten oxide	WO ₃	16	<i>Fd$\bar{3}m$</i>	10.270(3)	10.270(3)	10.270(3)	90	90	90
10815	Hydrogen tungstate	H _{0.23} WO ₃	2	<i>P4/nmm</i>	5.2285(5)	5.2285(5)	3.881(1)	90	90	90
11856	Hydrogen tungsten oxide	H _{0.5} WO ₃	1	<i>Pm$\bar{3}m$</i>	3.755	3.755	3.755	90	90	90
5480	Hydrogen tungsten oxide	H _{0.53} WO ₃	8	<i>Im$\bar{3}$</i>	7.562(2)	7.562(2)	7.562(2)	90	90	90
40821	Tungsten oxide hydrate	WO ₃ (H ₂ O) _{0.333}	12	<i>Fmm2</i>	7.3447(5)	12.5470(8)	7.7367(5)	90	90	90
47130	Tungsten trioxide hemihydrate	WO ₃ (H ₂ O) _{0.5}	16	<i>Fd$\bar{3}m$</i>	10.305(3)	10.305(3)	10.305(3)	90	90	90

* Coucou and Figlarz (1988).

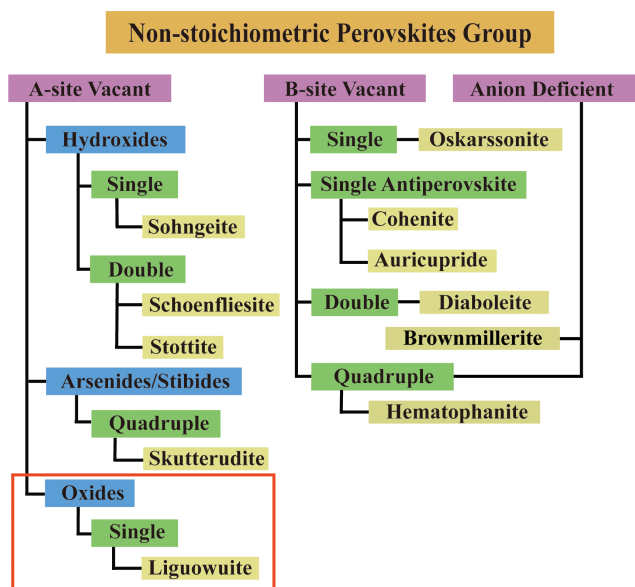
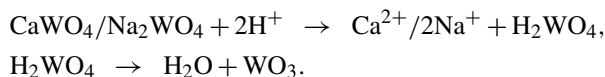


Figure 12. The suggested hierarchical category of the non-stoichiometric perovskite group minerals (modifications based on Mitchell et al., 2017). The mineral names in the yellow boxes refer to the subgroup names. The section highlighted in the red box is recommended in this article.

(Cortés-Jácome et al., 2005; Pan et al., 2006; Kanan and Tripp, 2007; Shang et al., 2020; Sirotkin et al., 2020; Song et al., 2020). The most common method of preparing nanoparticles of tungsten oxide is sol-gel synthesis, in which a tungstic acid (H₂WO₄) precursor is obtained by passing W-bearing materials (e.g., Na₂WO₄ or CaWO₄) through an ion-

exchange resin. Then, the resultant H₂WO₄ condenses in pure water to form an amorphous WO₃ network that is calcined at 180–800 °C, yielding *m*-WO₃ nanoparticles (Song et al., 2006; Kanan and Tripp, 2007; Li, 2013; Morajkar and Srinivasan, 2021), i.e.,



The liguowuite found in this study is naturally formed nano-monoclinic WO₃. From a mineralogical viewpoint, liguowuite was found in the same sample as scheelite, tellurite, tewite ((K_{1.5}□_{0.5})_{Σ2}(Te_{1.25}⁴⁺W_{0.25}□_{0.5})_{Σ2}W₅O₁₉), and wumuite (KA_{10.33}W_{2.67}O₉), which also contain K, Ca, W, and Te, indicating that the formation of these three new minerals may have been related to the same geological event. The trace amounts of K, Na, Ca, and Te in the liguowuite also convincingly indicate its natural origin. Considering the presence of scheelite, it can be reasonably speculated that in the natural metallogenic environment, the WO₄²⁻ groups reacted with an acidic hydrothermal solution to generate tungstic acid and the excess WO₄²⁻ groups reacting with Ca²⁺ ions to generate scheelite. Then, the tungstate acid was thermally decomposed into liguowuite and water.

As is shown in the BSE images (Fig. 2), the liguowuite exhibits triclinic pseudomorphism composed of nanoparticles. This is very similar to the process in which stokesite (CaSnSi₃O₉·2H₂O) crystals are heated to dehydrate and decompose into nano-sized mineral particles of cassiterite, malayaite, and cristobalite, but the original crystal morphologies of stokesite are preserved (Xue et al., 2016). Li (2013) studied the phase changes in the tungsten oxide and its hy-

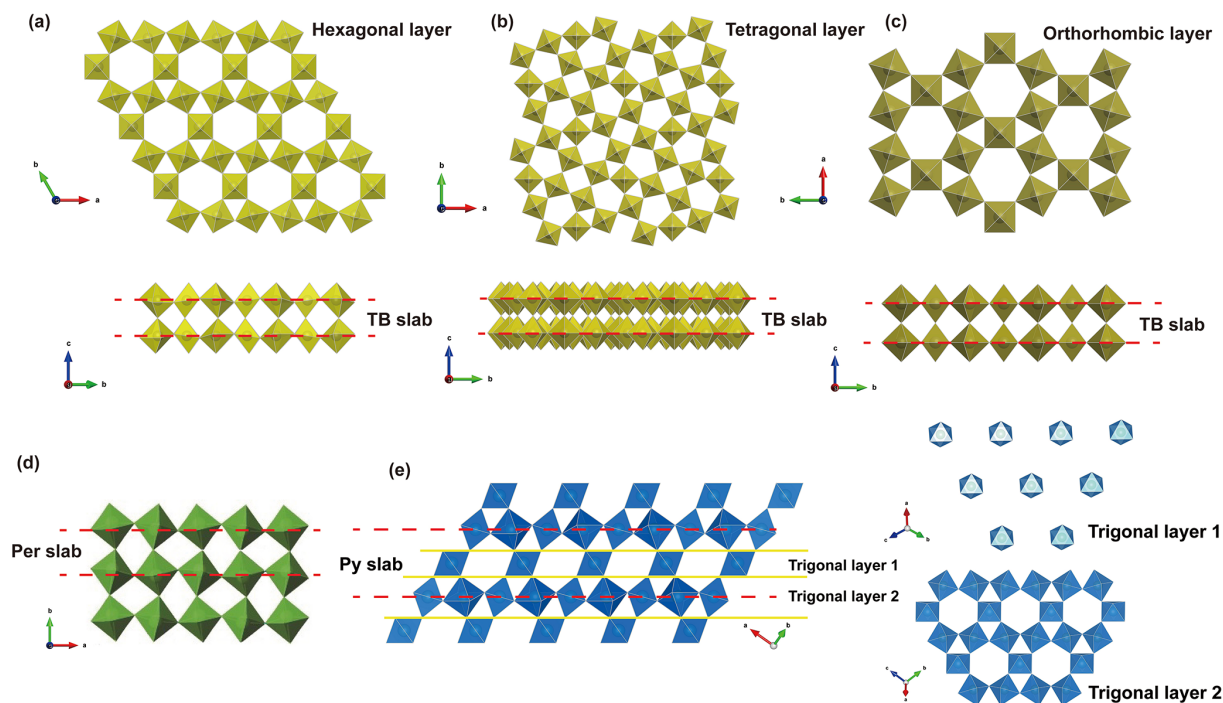


Figure 13. $[\text{WO}_6]$ octahedra framework for tungsten-bronze-type, perovskite-type, and pyrochlore-type structures. (a) Hexagonal tungsten bronze (HTB), (b) tetragonal tungsten bronze (TTB), (c) orthorhombic tungsten bronze (OTB), (d) perovskite-type structure (Per), (e) pyrochlore-type structure (Py). Pyrochlore slab is denoted by Py, while TB and perovskite slabs are indicated by TB and Per, respectively. A and Y sites are omitted for clarity.

drate products prepared through hydrothermal reactions under heated conditions ($> 140^\circ\text{C}$) and found that the structure of the tungsten oxide hydrate has a tendency to gradually lose H_2O molecules, and the mode of the water loss varies at different reaction temperatures. At low temperatures, the products tend to lose part of the H_2O molecules and undergo a phase transformation (i.e., $\text{WO}_3 \cdot \text{H}_2\text{O} \rightarrow \text{WO}_3 \cdot 0.33\text{H}_2\text{O}$). When the temperature increases, the H_2O molecules in the crystal structure totally escape, leaving a new WO_3 structure (i.e., $m\text{-WO}_3$).

During the mineralogical evolution, minerals can transform into another mineral and inherit its crystal structure (Krivovichev et al., 2013), such as the transformational series observed for the “zirsinalite $\text{Na}_6\text{CaZrSi}_6\text{O}_{18}$ — lovozerite $\text{Na}_3\text{CaZrSi}_6\text{O}_{15}(\text{OH})_3$ ” (Gerasimovskii, 1939; Khomyakov, 1977; Yamnova, et al., 2001) and “parakeldyshite $\text{Na}_2\text{ZrSi}_2\text{O}_7$ — keldyshite $\text{Na}_2\text{ZrSi}_2\text{O}_7$ ” (Khomyakov, 1977; Kabanova et al., 2020). It seems that liguowuite forms a similar series with H_2O -bearing WO_3 phases. Three hydrous tungsten oxide minerals have been described (Table 7) and may be related to the genesis of liguowuite. Therefore, it is speculated that the dehydration of a mineral containing W and volatiles leads to structural contraction and phase transformation, resulting in the preservation of WO_3 nanoparticles and changes in the crystal structure. In conclusion, the liguowuite found in this study

may have a natural thermal transformation origin, indicating that this W-containing mineral may be transformed via thermal activity after crystallization.

To explore the formation mechanism of the W-bearing minerals in this area, we also conducted a series of synthetic experiments. Wumuite was obtained from pure $m\text{-WO}_3$ and natural potassium feldspar (orthoclase) at 700°C (Xue et al., 2020), and tewite was successfully synthesized by mixing synthetic wumuite with $m\text{-WO}_3$ and TeO_2 , followed by heating at 650°C for 10 h (Li et al., 2019). These two reactions revealed that the wumuite and tewite probably crystallized from ore fluids at relatively high temperatures.

In addition, tellurite (TeO_2) crystals were also found among the associated minerals. The experimental results demonstrate that both TeO_2 and H_2WO_4 are volatile components at high temperatures. The experiments indicate that W can be transported in the form of $\text{K}_2\text{WO}_2\text{F}_4$ in acidic hydrothermal solutions and in the form of H_2WO_4 at high temperatures regardless of the pH of the solution (Zhao et al., 1977).

The hydrothermal-activity stage related to volcanism or magmatism is the most important enrichment and mineralization stage of tellurium. This series of new Te- and W-bearing minerals may have been formed by a high-temperature hydrothermal fluids rich in Te and W interspersed in the quartz monzonite in the early stage of the

Table 7. Data for comparison of liguowuite with related minerals.

Mineral species	Chemical formula	H ₂ O content	Crystal system	Space group	Crystal cell parameters	References
Liguowuite	WO ₃	0 wt %	Monoclinic	<i>P2₁/n</i>	$a = 7.32582(18) \text{ \AA}$, $b = 7.54767(18) \text{ \AA}$, $c = 7.71128(18) \text{ \AA}$, $\beta = 90.678(3)^\circ$, $V = 426.348(19) \text{ \AA}^3$, $Z = 8$	This work
Hydrotungstite	WO ₂ (OH) ₂ •H ₂ O	19.4 wt %	Monoclinic	<i>P2₁/m</i>	$a = 7.45 \text{ \AA}$, $b = 6.92 \text{ \AA}$, $c = 3.72 \text{ \AA}$, $\beta = 90.5^\circ$, $V = 191.77 \text{ \AA}^3$, $Z = 2$	Kerr and Young (1944)
Meymacite	WO ₃ •2H ₂ O	13.4 wt %	Amorphous			Pierrot and van Tassel (1965)
Tungstite	WO ₃ •H ₂ O	7.2 wt %	Orthorhombic	<i>Pmnb</i>	$a = 5.249 \text{ \AA}$, $b = 10.711 \text{ \AA}$, $c = 5.133 \text{ \AA}$, $V = 291.45 \text{ \AA}^3$, $Z = 4$	Szymanski and Roberts (1984)
“Krasnogorite”	WO ₃	0 wt %	Orthorhombic	<i>Pmnb</i>	$a = 7.39 \text{ \AA}$, $b = 7.53 \text{ \AA}$, $c = 3.84 \text{ \AA}$, $V = 213.68 \text{ \AA}^3$, $Z = 4$	Chesnokov et al. (1998)

Note: “krasnogorite” is an invalid mineral name.

gold mineralization. The liguowuite, wumuite, and tewite may have been formed in different stages of the hydrothermal fluid, were controlled by factors such as temperature and pH, and widely underwent metasomatic reactions.

Data availability. Crystallographic data for liguowuite (CIF) are available in the Supplement.

Supplement. The supplement related to this article is available online at: <https://doi.org/10.5194/ejm-34-95-2022-supplement>.

Author contributions. YX found the mineral. YX and NS made XRD analyses, determined physical and optical properties, and obtained spectroscopic data. HH and YY made TEM analyses. AC made Rietveld refinements. YX and NS prepared the manuscript with contributions from all co-authors.

Competing interests. The contact author has declared that neither they nor their co-authors have any competing interests.

Disclaimer. Publisher’s note: Copernicus Publications remains neutral with regard to jurisdictional claims in published maps and institutional affiliations.

Acknowledgements. We acknowledge Ritsuro Miyawaki, chairman of the CNMNC, and its members for their valuable suggestions on liguowuite. We also thank Chen Delin for his assistance during the fieldwork. Chemical analyses were carried out with the kind assistance of Ge Xiangkun, to whom we express our gratitude. In addition, we acknowledge the efforts of associate editor Sergey Krivovichev and of reviewers Taras L. Panikorovskii and Ian Grey for their detailed reviews.

Financial support. This research has been supported by the National Postdoctoral Program for Innovative Talents (grant no. BX20190304).

Review statement. This paper was edited by Sergey Krivovichev and reviewed by Ian Grey and Taras Panikorovskii.

References

- Akamatsu, T., Itoh, T., Izu, N., and Shin, W.: NO and NO₂ sensing properties of WO₃ and Co₃O₄ based gas sensors, *Sensors*, 13, 12467–12481, 2013.
- Brown, I. D.: Predicting bond lengths in inorganic crystals, *Acta Crystallogr.*, B33, 1305–1310, 1977.
- Bruker Optics: OPUS spectroscopy software, <https://www.bruker.com/products/infrared-near-infrared-and-raman-spectroscopy/opus-spectroscopy-software.html> (last access: 1 February 2022), 2019.
- Chen, Y. C., Yin, J. Z., Zhou, J. X., and Mao, J. W.: Geological characteristics of Dashuigou tellurium ore deposit in Shimian county, Sichuan province, China, *Sci. Geol. Sinica*, 29, 165–167, 1994.
- Chesnokov, B., Kotrly, M., and Nisanbajev, T.: Brennende Abraumhalden und Aufschlüsse im Tscheljabinsker Kohlenbecken – eine reiche Mineralienküche, *Mineralien-Welt*, 9, 54–63, 1998 (in German).
- Cortés-Jácome, M. A., Toledo, J. A., Angeles-Chavez, C., Aguilar, M., and Wang, J. A.: Influence of synthesis methods on tungsten dispersion, structural deformation, and surface acidity in binary WO₃–ZrO₂ system, *J. Phys. Chem. B*, 109, 22730–22739, 2005.
- Coucou, A. and Figlarz, M.: A new tungsten oxide with 3D tunnels: WO₃ with the pyrochlore-type structure, *Solid State Ionics*, 28–30, 1762–1765, 1988.
- Daniel, M. F., Desbat, B., Lassegues, J. C., Gerand, B., and Figlarz, M.: Infrared and Raman study of WO₃ tungsten trioxides and WO₃·xH₂O tungsten trioxide hydrates, *J. Solid State Chem.*, 67, 235–247, 1987.
- Evdokimova, O. L., Kusova, T. V., Polezhaeva, O., Shcherbakov, A. B., and Ivanov, V. K.: Highly reversible photochromism in composite WO₃/nanocellulose films, *Cellulose*, 26, 9095–9105, 2019.
- Farmer, V. C.: The infrared spectra of minerals, Chinese translation edition, Science Press, Beijing, 84 pp., ISBN 1303-12079, 1982.
- Francart, T., Van Wieringen, A., and Wouters, J.: APEX 3: A multi-purpose test platform for auditory psychophysical experiments, *J. Neurosci. Meth.*, 172, 283–293, <https://doi.org/10.1016/j.jneumeth.2008.04.020>, 2008.
- Gadsden, J. A.: Infrared spectra of minerals and related inorganic compounds, Butterworth, London, 152 pp., ISBN 0408-706651, 1975.
- Gerasimovskii, V. I.: Lovozerite a new mineral, *Doklady Akademii Nauk SSSR, American Mineral.*, 25, 753–756, 1939 (in Russian with English abstract).
- Gui, Y., Zhao, J., Wang, H., Tian, J., and Zhang, H.: Microwave-assisted gas–liquid interfacial synthesis of WO₃ precursor and nano-WO₃ for gas-sensing application, *J. Mater. Sci.-Mater. El.*, 27, 6445–6451, 2016.
- Guo, Y., Quan, X., Na, L. U., Zhao, H., and Chen, S.: High photocatalytic capability of self-assembled nanoporous WO₃ with preferential orientation of (002) planes, *Environ. Sci. Technol.*, 41, 4422–4427, 2007.
- Hong Q. M., Zhou, Z. H., and Hu S. Z.: Study on the Bond Valence Parameters for Tungsten-oxygen Bonds, *Acta Chim. Sinica*, 62, 1733–1737, 2004.
- Hyde, B. G. and Andersson, S.: Inorganic crystal structures, Wiley Interscience, New York, 302 pp., ISBN 0471-628972, 1989.
- Kabanova, N. A., Panikorovskii, T. L., Shilovskikh, V. V., Vlasenko, N. S., Yakovenchuk, V. N., Aksenov, S. M., Bocharov, V. N., and Krivovichev, S. V.: The Na_{2–n}H_n[Zr(Si₂O₇)]·m H₂O Minerals and Related Compounds (*n* = 0–0.5; *m* = 0.1): Structure Refinement, Framework Topology, and Possible Na⁺-Ion Migration Paths, *Crystals*, 10, 1016, <https://doi.org/10.3390/cryst10111016>, 2020.
- Kanan, S. M. and Tripp, C. P.: Synthesis, FTIR studies and sensor properties of WO₃ powders, *Curr. Opin. Solid St. M.*, 11, 19–27, 2007.
- Kerr P. F. and Young F.: Hydrotungstite, a new mineral from Oruro, Bolivia, *Am. Mineral.*, 29, 192–210, 1944.
- Khadayate, R. S., Sali, J. V., and Patil, P. P.: Acetone vapor sensing properties of screen printed WO₃ thick films, *Talanta*, 72, 1077–1081, 2007.
- Khomyakov, A. P.: New data on mineralogy of lovozerite group, *Dokl. Akad. Nauk SSSR+*, 237, 199–202, 1977.
- Krivovichev, S. V.: Structural complexity of minerals: information storage and processing in the mineral world, *Mineral. Mag.*, 77, 275–326, 2013.
- Larson, A. C. and Von Dreele, R. B.: GSAS – General Structure Analysis System, Los Alamos National Laboratory Report LAUR, 86–748, available electronically by anonymous ftp from <ftp://ftp.mist.lansce.lanl.gov> (last access: 4 February 2022), 1994.
- Laugier, J. and Bochu, B.: CHECKCELL – A Software Performing Automatic Cell/Space Group Determination, Collaborative Computational Project Number 14 (CCP14), Laboratoire des Matériaux et du Génie Physique de l’Ecole Supérieure de Physique de Grenoble (INPG), France, 2000.
- Li, J. Y.: Study of controlled synthesis of WO₃·nH₂O micro/nanomaterials and their properties, PhD thesis, Shanxi University of Science and Technology, <https://doi.org/10.7666/d.D441989>, 2013.
- Li, G. W., Xue, Y., and Xiong, M.: Tewite: A K–Te–W new mineral species with a modified tungsten-bronze type structure, from the Panzhuhua–Xichang region, southwest China, *Eur. J. Mineral.*, 31, 145–152, 2019.
- Li, X. L., Lou, T. J., Sun, X. M., and Li, Y. D.: Highly sensitive WO₃ hollow-sphere gas sensors, *Inorg. Chem.*, 43, 5442–5449, 2004.
- Mandarin, J. A.: The Gladstone-Dale relationship: Part IV. The compatibility concept and its application, *Can. Mineral.*, 19, 441–450, 1981.
- Martínez, A., Prieto, G., Arribas, M. A., Concepción, P., and Sánchez-Royo, J. F.: Influence of the preparative route on the properties of WO_x–ZrO₂ catalysts: a detailed structural, spectroscopic, and catalytic study, *J. Catal.*, 248, 288–302, 2007.
- Mitchell, R., Welch, M. D., and Chakhmouradian, A. R.: Nomenclature of the perovskite supergroup: a hierarchical system of classification based on crystal structure and composition, *Mineral. Mag.*, 81, 411–461, 2017.
- Miyazaki, H., Ishigaki, T., Suzuki, H., and Ota, T.: Effect of film thickness and air atmosphere on photochromic properties of WO₃ based composite films, *B. Chem. Soc. Jpn.*, 89, 20–23, 2015.
- Morajkar, S. M. and Srinivasan, B. R.: Synthesis, spectral and structural characterization of organic ammonium paratungstates, *Indian J. Chem. A*, 60, 185–195, 2021.

- Oxford Cryosystems Ltd.: Crystallographica Search-Match, *J. Appl. Crystallogr.*, 32, 379–380, <https://doi.org/10.1107/S0021889899004124>, 1999.
- Pan, J. H. and Lee, W. I.: Preparation of highly ordered cubic mesoporous WO₃/TiO₂ films and their photocatalytic properties, *Chem. Mater.*, 18, 847–853, 2006.
- Pierrot, R. and van Tassel, R.: Nouvelle définition de la meymacite et nomenclature de “acides tungstiques” naturels, *B. Soc. Fr. Mineral Cr.*, 88, 613–617, 1965.
- Poirier, G., Nalin, M., Messaddeq, Y., and Ribeiro, S.: Photochromic properties of tungstate-based glasses, *Solid State Ionics*, 178, 871–875, 2007.
- Reyes, L. F., Hoel, A., Saukko, S., Heszler, P., and Granqvist, C. G.: Gas sensor response of pure and activated WO₃ nanoparticle films made by advanced reactive gas deposition, *Sensor Actuator*, B117, 128–134, 2006.
- Shang, J., Xiao, Z., Yu, L., Aprea, P., and Hao, S.: An insight on the role of PVP in the synthesis of monoclinic WO₃ with efficiently photocatalytic activity, *Nanotechnology*, 31, 125603, <https://doi.org/10.1088/1361-6528/ab5c4f>, 2020.
- Sirotkin, N. A., Khlyustova, A. V., Titov, V. A., Krayev, A. S., and Agafonov, A. V.: Synthesis and photocatalytic activity of WO₃ nanoparticles prepared by underwater impulse discharge, *Plasma Chem. Plasma P.*, 40, 1–17, 2020.
- Song, W. Q., Zhang, R., Bai, X., Jia, Q. Q., and Ji, H. M.: Exposed crystal facets of WO₃ nanosheets by phase control on NO₂-sensing performance, *J. Mater. Sci.-Mater. El.*, 31, 610–620, 2020.
- Song, X. C., Zhao, Y., and Zheng, Y. F.: Hydrothermal synthesis of tungsten oxide nanobelts, *Mater. Lett.*, 60, 3405–3408, 2006.
- Szymanski, J. T. and Roberts, A. C.: The crystal structure of tungstite, WO₃·H₂O, *Can. Mineral.*, 22, 681–688, 1984.
- Tian, F. H., Zhao, L. H., Xue, X. Y., Shen, Y. Y., Jia, X. F., Chen, S. G., and Wang, Z. H.: DFT study of CO sensing mechanism on hexagonal WO₃ (001) surface: The role of oxygen vacancy, *Appl. Surf. Sci.*, 311, 362–368, 2014.
- Xue, Y., Li, G. W., and Xing, X. L.: Thermodynamic and crystallographic studies of phase transition of stokesite, in: *National Symposium on Mineral Science and Engineering*, Beijing, 21–23 October, 2016, 24–25, 2016.
- Xue, Y., Li, G., and Xie, Y.: Wumuite (KAl_{0.33}W_{2.67}O₉) – a new mineral with an HTB-type structure from the Panzhihua–Xichang region in China, *Eur. J. Mineral.*, 32, 483–494, <https://doi.org/10.5194/ejm-32-483-2020>, 2020.
- Yamnova, N. A., Egorov-Tismenko, Y. K., and Pekov, I. V.: Refined crystal structure of lovozerite Na₂CaZr[Si₆O₁₂(OH,O)₆]·H₂O, *Crystallogr. Rep.*, 46, 937–941, 2001.
- Yang, T. S., Zhang, Y., Cai, Y. A., and Tian, H.: Effect of processing parameters on anodic nanoporous tungsten oxide film structure and porosity for hydrogen detection, *J. Mater. Res.*, 29, 166–174, 2014.
- Zhao, B., Li, W. X., and Cai, Y. J.: Conditions of formation of wolframite, cassiterite, columbite, microlite and tapiolite and experimental studies on the variation of Nb and Ta in wolframite and cassiterite, *Geochimica*, 2, 123–136, 1977 (in Chinese).